J. Fluid Mech. (2001), *vol.* 444, *pp.* 383–407. Printed in the United Kingdom

Boundary layer leading-edge receptivity to sound at incidence angles

By ERCAN ERTURK[1] AND THOMAS C. CORKE[2]

[1]College of Engineering, Gebze Institute of Technology, Gebze, Kocaeli 41400, Turkey

[2]Department of Aerospace and Mechanical Engineering, University of Notre Dame, IN 46556, USA

(Received 24 April 2000 and in revised form 16 April 2001)

The leading-edge receptivity to acoustic waves of two-dimensional parabolic bodies was investigated using a spatial solution of the Navier–Stokes equations in vorticity/streamfunction form in parabolic coordinates. The free stream is composed of a uniform flow with a superposed periodic velocity fluctuation of small amplitude. The method follows that of Haddad & Corke (1998) in which the solution for the basic flow and linearized perturbation flow are solved separately. We primarily investigated the effect of frequency and angle of incidence ($-180^\circ \leqslant \alpha_2 \leqslant 180^\circ$) of the acoustic waves on the leading-edge receptivity. The results at $\alpha_2 = 0^\circ$ were found to be in quantitative agreement with those of Haddad & Corke (1998), and substantiated the Strouhal number scaling based on the nose radius. The results with sound waves at angles of incidence agreed qualitatively with the analysis of Hammerton & Kerschen (1996). These included a maximum receptivity at $\alpha_2 = 90^\circ$, and an asymmetric variation in the receptivity with sound incidence angle, with minima at angles which were slightly less than $\alpha_2 = 0^\circ$ and $\alpha_2 = 180^\circ$.

1. Introduction

Transition from laminar flow to turbulent flow is still one of the basic and important technologically relevant fluid mechanics problems. The transition process begins with the disturbances in the free stream entering the boundary layer and exciting instability modes within the boundary layer. At this stage the process is called 'receptivity', which is a term first introduced by Morkovin (1969). For a Blasius flow these instability modes are the Tollmien–Schlichting (T–S) modes. In predicting the transition location, it is essential to know the initial amplitudes of the T–S waves at the leading edge. The receptivity coefficient relates the initial amplitude of the T–S waves to the amplitude of the free-stream disturbance.

Receptivity phenomena can be classified into two groups: vortical receptivity and acoustic receptivity. Examples of vortical receptivity can be the generation of instability waves by a vibrating ribbon, unsteady wall suction or blowing and unsteady wall heating or cooling. In vortical receptivity, the input disturbances generally produce a fluctuating velocity or vortical component which can directly couple with the fluid instability wave. The situation is rather different in acoustic receptivity in incompressible flows. Acoustic receptivity refers to coupling between boundary layer instabilities and free-stream sound. Assuming that the disturbances are weak enough so that the receptivity process is linear in the disturbance amplitude, the instability

waves generated in the boundary layer have the same frequency as the external acoustic disturbance; however the wavelengths of the acoustic disturbances are much longer than those of the instability waves. Therefore in order to transfer energy from the external acoustic disturbances to the instability waves, a wavelength conversion mechanism is required. This is the essence of acoustic receptivity for incompressible flows, which only recently has been fully appreciated and understood.

The theoretical framework of receptivity phenomena was first constructed by Goldstein (1983). His study on flat-plate boundary layers showed that the energy transfer from long-wavelength free-stream oscillations to short-wavelength boundary layer instability waves occurs at the leading edge, where there is a sharp change in the wall curvature which results in a rapid streamwise change in the mean flow, and a sharp peak in the mean vorticity.

Hammerton & Kerschen (1992) used an asymptotic analysis to study the acoustic receptivity of boundary layers on parabolic bodies. In their formulation, the effect of the leading-edge sharpness is represented by a Strouhal number based on the frequency of the acoustic disturbance and the nose radius of curvature. Their results showed that the leading-edge receptivity coefficient is a strong function of this Strouhal number. Later Hammerton & Kerschen (1996) examined the effect of the angle of incidence of the acoustic disturbances on the receptivity. Their results indicated that the leading-edge receptivity coefficient increased as the sound incidence angle increased, reaching a maximum at 90°. Beyond that angle, the receptivity coefficient decreased, with minima occurring at angles which were slightly less than 0° and 180°.

Murdock (1981) used a spectral numerical method to model the unsteady flow and growth of instabilities due to a periodic free-stream oscillation of the flow over parabolic cylinders. He determined the effect at the leading edge by fitting a curve to the modulus of the streamwise amplitude distribution and extrapolating upstream to the leading edge. He also found the leading-edge receptivity coefficient to increase as the leading-edge radius decreased.

A more recent numerical simulation of the leading-edge receptivity was done by Haddad & Corke (1998). This involved an efficient spatial formulation of the linearized Navier–Stokes equations. They also examined the flow over parabolic bodies with different nose radii of curvature. With this, they considered only a limited number of acoustic frequencies which were selected to match those of Lin, Reed & Saric (1990). Their results showed the same dependence of the leading-edge receptivity coefficient on the leading-edge radius as was found by Murdock (1981) and Hammerton & Kerschen (1992). They also found good quantitative agreement with the experimental leading-edge receptivity coefficient of Saric, Wei & Rasmussen (1994).

2. Objective

The objective of this work was to continue the use of the efficient spatial formulation of Haddad & Corke (1998), and expand their results by (i) examining a considerably broader range of frequencies of acoustic disturbances that would allow a more complete check on the applicability of the receptivity dependence on the Strouhal number based on the nose radius and acoustic frequency, and (ii) examining the effect of the acoustic disturbance angle of incidence, which was shown to have a dramatic influence on the leading-edge receptivity in the asymptotic analysis of Hammerton & Kerschen (1996).

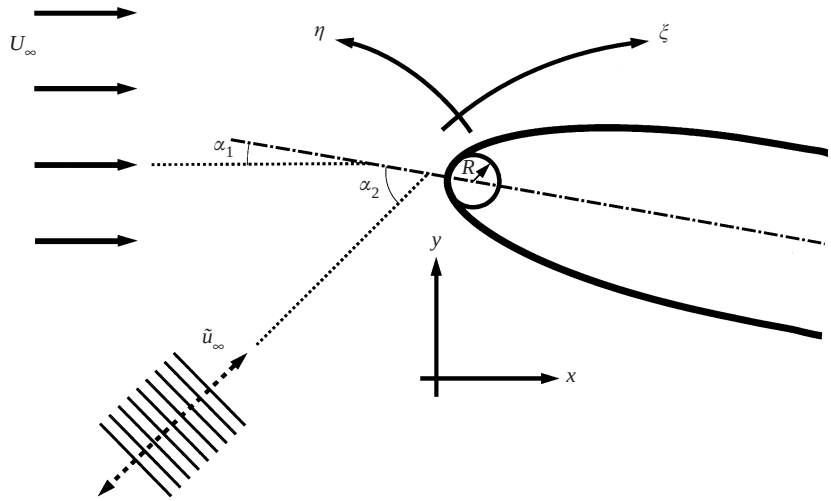

FIGURE 1. Schematic view of the physical problem.

3. Physical problem

A schematic view of the physical problem considered is illustrated in figure 1. The mathematical equation of the parabolic body is given by

$$x(y) = \frac{1}{2R}(y^2 - R^2), \tag{3.1}$$

where x and y are the Cartesian coordinates, and R is the nose radius of curvature of the parabolic body.

3.1. *Governing equations*

The governing equations of the problem are the full Navier–Stokes (N–S) equations. Following Davis (1972) and Haddad & Corke (1998), we write them in terms of streamfunction (ψ) and vorticity (ω). In dimensional form these are given as

$$\frac{\partial^2 \psi^*}{\partial x^{*2}} + \frac{\partial^2 \psi^*}{\partial y^{*2}} = -\omega^*, \tag{3.2}$$

$$\frac{\partial \omega^*}{\partial t^*} + \frac{\partial \psi^*}{\partial y^*}\frac{\partial \omega^*}{\partial x^*} - \frac{\partial \psi^*}{\partial x^*}\frac{\partial \omega^*}{\partial y^*} = \nu\left(\frac{\partial^2 \omega^*}{\partial x^{*2}} + \frac{\partial^2 \omega^*}{\partial y^{*2}}\right), \tag{3.3}$$

where superscript * denotes dimensional terms. We non-dimensionalize the variables using the free-stream velocity (U_∞) and viscosity (ν) such that

$$x = \frac{x^*}{\nu/U_\infty}, \quad y = \frac{y^*}{\nu/U_\infty}, \quad t = \frac{t^*}{\nu/U_\infty^2}, \quad \omega = \frac{\omega^*}{U_\infty^2/\nu}, \quad \psi = \frac{\psi^*}{\nu}. \tag{3.4}$$

Since we are dealing with a parabolic body, the natural choice is to use parabolic instead of Cartesian coordinates. The relation between the dimensionless Cartesian coordinates (x, y) and the dimensionless parabolic coordinates (ξ, η) is given by

$$x = \frac{\xi^2 - \eta^2}{2}, \quad y = \xi\eta. \tag{3.5}$$

Incorporating these, the dimensionless governing equations in parabolic coordinates

are

$$\frac{\partial^2\psi}{\partial\xi^2}+\frac{\partial^2\psi}{\partial\eta^2}=-(\xi^2+\eta^2)\omega, \tag{3.6}$$

$$-(\xi^2+\eta^2)\frac{\partial\omega}{\partial t}+\frac{\partial^2\omega}{\partial\xi^2}+\frac{\partial^2\omega}{\partial\eta^2}+\frac{\partial\psi}{\partial\xi}\frac{\partial\omega}{\partial\eta}-\frac{\partial\psi}{\partial\eta}\frac{\partial\omega}{\partial\xi}=0. \tag{3.7}$$

This is the final form of our equations. We did not utilize the additional transformation used by Davis (1972) and Haddad & Corke (1998) to maintain a finite vorticity at the leading edge for a case when $R=0$. We note that for an infinitely thin flat plate ($R=0$), these equations are singular at the leading edge ($\xi=0,\eta=0$). Therefore in this study, we will always consider the cases where $R>0$.

3.2. *Boundary conditions*

In parabolic coordinates, the wall of the parabolic body is defined by a constant-η line, such as

$$\eta_{wall}=R^{1/2}, \tag{3.8}$$

where R is the radius of curvature at the leading edge. Since we use a viscous length scale in the non-dimensionalization, R can be considered as the Reynolds number based on the nose radius of curvature. Similarly, every physical length, when non-dimensionalized, will be a Reynolds number based on that physical length.

3.2.1. *Wall boundary conditions*

Streamfunction: the wall is defined by a streamline with a streamfunction value being an arbitrary constant. We choose to set it to zero, namely

$$\psi=\text{constant}=0 \quad \text{at} \quad \eta=R^{1/2}. \tag{3.9}$$

Also on the wall, the no-slip, no-penetration boundary condition requires

$$\frac{\partial\psi}{\partial\eta}=0 \quad \text{at} \quad \eta=R^{1/2}. \tag{3.10}$$

Vorticity: there is no explicit boundary condition for defining vorticity on the wall. Therefore we will use the streamfunction equation applied at the wall as the boundary condition for vorticity. Given the streamfunction equation

$$\frac{\partial^2\psi}{\partial\xi^2}+\frac{\partial^2\psi}{\partial\eta^2}=-\left(\xi^2+\eta^2\right)\omega \tag{3.11}$$

and the conditions on the wall, $\psi=0$, giving $\psi_\xi=\psi_{\xi\xi}=0$, the condition that relates vorticity and streamfunction at the wall is

$$\omega=\left(\frac{-1}{\xi^2+\eta^2}\right)\psi_{\eta\eta} \quad \text{at} \quad \eta=R^{1/2}. \tag{3.12}$$

3.2.2. *Free-stream boundary conditions*

Streamfunction: we have used the free-stream velocity in normalization, therefore at the free stream the magnitude of the velocity is equal to unity, namely

$$|U|=1. \tag{3.13}$$

Then the velocity components in the free stream will be

$$u=\cos(\alpha), \quad v=\sin(\alpha), \tag{3.14}$$

where u and v are the respective velocity components in the x- and y-directions, and α is the angle of the free-stream velocity with respect to the body. Since the streamfunction is defined as

$$\frac{\partial \psi}{\partial y} = u \quad \text{and} \quad \frac{\partial \psi}{\partial x} = -v \tag{3.15}$$

at the free stream, the value of the streamfunction is defined as

$$\psi_\infty = y\cos(\alpha) - x\sin(\alpha), \tag{3.16}$$

where x and y are the Cartesian coordinates. Hence using parabolic coordinates, the free-stream boundary condition for the streamfunction is

$$\frac{\partial \psi}{\partial \eta} \to \xi\cos(\alpha) + \eta\sin(\alpha) \quad \text{as} \quad \eta \to \infty. \tag{3.17}$$

Vorticity: away from the wall, the potential flow has zero vorticity. Therefore

$$\omega \to 0 \quad \text{as} \quad \eta \to \infty. \tag{3.18}$$

4. Basic flow and perturbation flow equations

To investigate the leading-edge receptivity, we use a spatial approach. This has the advantage of numerically calculating variables with different orders of magnitude to greater accuracy. With this approach, the acoustic disturbance is represented as a periodic, small-amplitude perturbation on the uniform free-stream flow, namely

$$\psi = \psi_\infty + \epsilon e^{i\sigma t}\tilde{\psi}_\infty \tag{4.1}$$

where σ is the temporal frequency, and ϵ is the amplitude of the perturbation, which is sufficiently small for linearization.

As illustrated in figure 1, the mean flow and acoustic waves can be at incidence angles with respect to the body. Therefore

$$\psi = (\xi\cos(\alpha_1) + \eta\sin(\alpha_1)) + \epsilon e^{i\sigma t}(\xi\cos(\alpha_2) + \eta\sin(\alpha_2)) \tag{4.2}$$

where α_1 is the angle of attack of the parabolic body with respect to the free-stream streamline, and α_2 is the angle of incidence of acoustic waves with respect to the body centreline.

Following this, the governing (N–S) equations for streamfunction and vorticity are converted into two sets of equations, governing the mean (basic) flow and perturbation flows. This is done by writing the total flow quantities as the sum of the mean (time-independent) quantities, Ψ and Ω, and the perturbation quantities, $\tilde{\psi}$ and $\tilde{\omega}$:

$$\psi(\xi,\eta,t) = \Psi(\xi,\eta) + \epsilon e^{i\sigma t}\tilde{\psi}(\xi,\eta), \tag{4.3}$$

$$\omega(\xi,\eta,t) = \Omega(\xi,\eta) + \epsilon e^{i\sigma t}\tilde{\omega}(\xi,\eta), \tag{4.4}$$

Substituting these into the governing equations (3.6) and (3.7) leads to the equations for the basic flow (order ϵ^0), which are

$$\frac{\partial^2 \Psi}{\partial \xi^2} + \frac{\partial^2 \Psi}{\partial \eta^2} = -(\xi^2 + \eta^2)\Omega, \tag{4.5}$$

$$\frac{\partial^2 \Omega}{\partial \xi^2} + \frac{\partial^2 \Omega}{\partial \eta^2} + \frac{\partial \Psi}{\partial \xi}\frac{\partial \Omega}{\partial \eta} - \frac{\partial \Psi}{\partial \eta}\frac{\partial \Omega}{\partial \xi} = 0, \tag{4.6}$$

with the boundary conditions

$$\Psi = 0, \quad \frac{\partial \Psi}{\partial \eta} = 0, \quad \Omega = \left(\frac{-1}{\xi^2 + \eta^2}\right) \frac{\partial^2 \Psi}{\partial \eta^2} \quad \text{at} \quad \eta = R^{1/2}, \tag{4.7}$$

$$\frac{\partial \Psi}{\partial \eta} \to \xi \cos(\alpha_1) + \eta \sin(\alpha_1), \quad \Omega \to 0 \quad \text{at} \quad \eta \to \infty, \tag{4.8}$$

and the equations for the perturbation flow (order ϵ^1), which are

$$\frac{\partial^2 \tilde{\psi}}{\partial \xi^2} + \frac{\partial^2 \tilde{\psi}}{\partial \eta^2} = -(\xi^2 + \eta^2)\tilde{\omega}, \tag{4.9}$$

$$-\mathrm{i}\sigma(\xi^2 + \eta^2)\tilde{\omega} + \frac{\partial^2 \tilde{\omega}}{\partial \xi^2} + \frac{\partial^2 \tilde{\omega}}{\partial \eta^2} + \frac{\partial \Psi}{\partial \xi}\frac{\partial \tilde{\omega}}{\partial \eta} + \frac{\partial \Omega}{\partial \eta}\frac{\partial \tilde{\psi}}{\partial \xi} - \frac{\partial \Psi}{\partial \eta}\frac{\partial \tilde{\omega}}{\partial \xi} - \frac{\partial \Omega}{\partial \xi}\frac{\partial \tilde{\psi}}{\partial \eta} = 0, \tag{4.10}$$

with the boundary conditions

$$\tilde{\psi} = 0, \quad \frac{\partial \tilde{\psi}}{\partial \eta} = 0, \quad \tilde{\omega} = \left(\frac{-1}{\xi^2 + \eta^2}\right) \frac{\partial^2 \tilde{\psi}}{\partial \eta^2} \quad \text{at} \quad \eta = R^{1/2}, \tag{4.11}$$

$$\frac{\partial \tilde{\psi}}{\partial \eta} \to \xi \cos(\alpha_2) + \eta \sin(\alpha_2), \quad \tilde{\omega} \to 0 \quad \text{at} \quad \eta \to \infty. \tag{4.12}$$

Note that the equations for the basic flow are nonlinear, and therefore require an iterative numerical method for their solution. The basic flow variables are real, and the equations have a real solution. On the other hand, the equations for the perturbation flow are linear, and therefore can be solved numerically with a direct linear solver. The perturbation variables are however complex, and the equations have a complex solution. We also note that the temporal frequency σ appears explicitly in the equations for the perturbation flow, thus the solution is expected to be frequency dependent.

To understand the receptivity problem, we have used this spatial approach. For this, we are interested in the streamwise variation of the amplitude of the perturbation that couples with the T–S waves of the same frequency. By considering the perturbation amplitudes to be linear, and using this normal mode form, the basic flow and perturbation flow can be solved separately to the same order of accuracy. This approach then allows us to perform more precise numerical calculations on the perturbation values, and minimize any numerical truncation errors.

5. Grid generation

The contour of the body is defined by the line $\eta_{wall} = R^{1/2}$. The free stream is also defined by the line $\eta = \eta_{max}$. We set the free stream to be at a distance from the wall that is at least ten times the expected boundary layer thickness. Therefore in the wall-normal direction we let η vary between the values

$$R^{1/2} \leqslant \eta \leqslant R^{1/2} + 35. \tag{5.1}$$

In the η-direction we have used 36 grid points.

In the streamwise direction,

$$-\xi_{max} \leqslant \xi \leqslant +\xi_{max}. \tag{5.2}$$

On the surface of the body, the leading edge is located at $\xi = 0$. The outflow

boundaries on the lower and upper sides of the body in the physical plane are located at $\xi = -\xi_{max}$ and $\xi = +\xi_{max}$ in the numerical plane. In the domains between $\xi = 0$ and $\xi = \mp\xi_{max}$, we have used 1001 grid points. This gave a minimum of 10 points per T–S wavelength. We set the last grid point in ξ-direction to be located at $x_{max} = 1.5 \times 10^6$ (including the buffer zone which will be explained later in this section). Therefore, the last grid point in the streamwise direction was located at

$$\xi_{max} = (2x_{max} + R)^{1/2}. \tag{5.3}$$

In order to capture the physical phenomenon more accurately, more grid points were located near the wall in η-direction, and near the leading edge in ξ-direction. This was done using Robert's stretching transformation of the original uniform grid (Anderson, Tannehill & Pletcher 1984). The formula of the transformation is

$$y = h\frac{(\beta+1) - (\beta-1)[(\beta+1)/(\beta-1)]^{1-\bar{y}}}{[(\beta+1)/(\beta-1)]^{1-\bar{y}} + 1}, \tag{5.4}$$

where $\bar{y}$ represents the original uniformly spaced grid points, y are the stretched grid points and β is the stretching parameter. In our case we used $\beta_\xi = 1.05$ and $\beta_\eta = 1.005$ which produced the accuracy we desired.

The geometry we are dealing with is a semi-infinite body. Since the numerical calculations cover a finite domain, the buffer domain technique used by Haddad & Corke (1998) was used to provide the outflow boundary condition. The approach is to gradually kill the elliptic $(\partial^2/\partial\xi^2)$ terms in the governing equations in a buffer zone at the downstream end of the computational domain. To accomplish this, these elliptic terms were multiplied by a weighting factor s. At the beginning of the buffer zone, $s = 1$. At the end of the buffer zone, $s = 0$. In between, the s changes according to

$$s(i) = \frac{\tanh(4) + \tanh(\arg)}{2\tanh(4)} \tag{5.5}$$

where

$$\arg = 4\left(1 - \frac{2(i - i_{buf})}{(i_{max} - i_{buf})}\right) \tag{5.6}$$

and i is the numerical streamwise index, i_{max} is the numerical index of the last grid point in the streamwise direction, and i_{buf} is the index (i) of the first grid point at the beginning of the buffer zone. The length of the buffer zone corresponded to approximately 5 T–S wavelengths, which was well beyond the minimum of 3 given by Haddad & Corke (1998).

6. Numerical method

For the solution of the nonlinear steady basic flow equations, we developed an iterative numerical method. The basic flow variables are improved through a pseudo-time marching until convergence is achieved (Erturk 1999; Erturk & Corke 2001). For the solution of the linear perturbation equations, we used an efficient direct linear solver (LINPACK subroutines). The solution methodology of the problem is to first solve the basic flow equations. Using the basic flow solution, the coefficients in the perturbation equations were next calculated. With specified values of the frequency, σ, and angle of incidence of the acoustic waves, α_2, the perturbation equations are then solved. In the results presented here, the angle of incidence of the body, α_1, was always zero.

For the numerical solution of the perturbation equations, we used the same numerical grid and buffer zone that was used for the solution of the basic flow equations. We note that all the results that were presented here are grid independent.

7. Results and discussion

7.1. *Basic flow solutions*

In order to make a quantitative check of our numerical solutions, we compared the wall skin friction and surface pressure distributions for a family of parabolas with different nose radii, to those of Haddad & Corke (1998). We note that by comparing our basic flow solutions with theirs, we indirectly also compare our results to those of Davis (1972), which agreed with those of Haddad & Corke (1998).

The skin friction coefficient is defined as

$$C_f = \frac{\tau_w^*}{\rho U_\infty^2} \tag{7.1}$$

where $\tau_w^* = \mu(\partial u^*/\partial y^*)|_w$. If we write the above equation in terms of the non-dimensional streamfunction variable and use the streamfunction equation at the wall, we obtain

$$C_f = -\Omega|_w . \tag{7.2}$$

Haddad & Corke (1998) followed Davis (1972) and scaled the above equation with $(\xi^2+\eta^2)/\xi$. Using the same approach, our scaled skin friction coefficient has the form

$$C_f = \frac{-\left(\xi^2+\eta^2\right)}{\xi}\Omega(\xi, R^{1/2}). \tag{7.3}$$

Figure 2 shows the scaled skin friction distribution over parabolic bodies with different nose radii. The skin friction is a maximum at the leading edge for any particular parabolic body, and increase as the nose radius (Reynolds number) increase. Davis (1972) pointed out that the flow over a parabolic body asymptotically approaches Blasius flow away from the leading edge. As a check on the numerical solution, the skin friction coefficient for a Blasius flow is shown by the dotted line. As can be seen, all of the skin friction distributions asymptote to the Blasius value downstream of the leading edge. The symbols correspond to the results from Haddad & Corke (1998).

In order to obtain an expression for the surface pressure distribution, we start with the x^*-momentum equation (in dimensional variables):

$$u^*\frac{\partial u^*}{\partial x^*} + v^*\frac{\partial u^*}{\partial y^*} = -\frac{1}{\rho}\frac{\partial p^*}{\partial x^*} + \nu\left[\frac{\partial^2 u^*}{\partial x^{*2}} + \frac{\partial^2 u^*}{\partial y^{*2}}\right]. \tag{7.4}$$

We apply the boundary conditions at the wall, that is $u^* = v^* = 0$. Also, we introduce the streamfunction as $u^* = \partial\Psi^*/\partial y^*$. When we non-dimensionalize the pressure to be in the form $p = (p^* - p^*_{\xi=-\infty})/(\rho U_\infty^2)$, and use the streamfunction equation, the momentum equation (7.4) takes the following form in parabolic coordinates:

$$\frac{\partial p}{\partial \xi} = -\frac{\partial \Omega}{\partial \eta}. \tag{7.5}$$

This equation relates the pressure gradient to the vorticity variable. Haddad & Corke (1998) followed Davis (1972) and instead of using streamfunction and vorticity variables in the governing equations, they used transformed variables in order to remove the singularity that occurs at the leading edge in the case of an infinitely thin

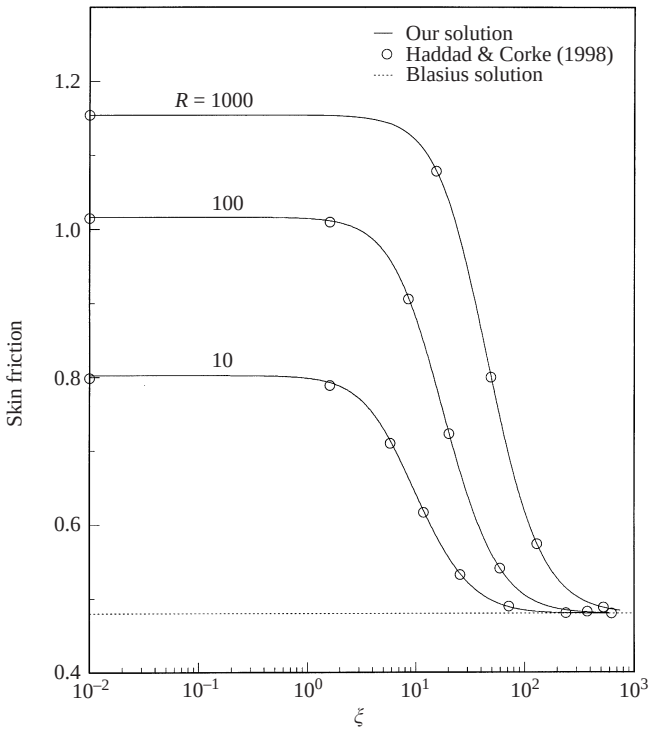

FIGURE 2. Skin friction distribution on parabolic bodies.

flat plate. In order to compare our results with theirs, we also used the transformed variables. Thus following Davis (1972),

$$P = p - \frac{\eta}{(\xi^2 + \eta^2)} g(0, R^{1/2}), \tag{7.6}$$

where g is the transformed vorticity variable, and is related to vorticity by

$$g(\xi, \eta) = \frac{-(\xi^2 + \eta^2)}{\xi} \Omega(\xi, \eta). \tag{7.7}$$

Substituting equation (7.6) into equation (7.5) we obtain

$$\frac{\partial P}{\partial \xi} = -\frac{\partial \Omega}{\partial \eta} + \frac{2\xi\eta}{(\xi^2 + \eta^2)^2} g(0, R^{1/2}). \tag{7.8}$$

We use the pressure at downstream infinity on the lower surface as a reference pressure, and integrate the above equation back along the surface using the trapezoidal method.

Figure 3 shows the pressure distribution obtained for parabolic bodies with different nose radii. As can be seen, the pressure gradient is favourable everywhere, meaning that the pressure gradient is stabilizing everywhere in terms of T–S instabilities. The pressure is a maximum at the stagnation point (i.e. at the leading edge) and decreases monotonically to zero far downstream. Again the agreement with Haddad & Corke (1998) is excellent.

The method that we developed for the solution of two-dimensional incompressible steady N–S equations has proved to be very effective. The results were found to agree well with those of Haddad & Corke (1998) (and thereby Davis 1972), and far

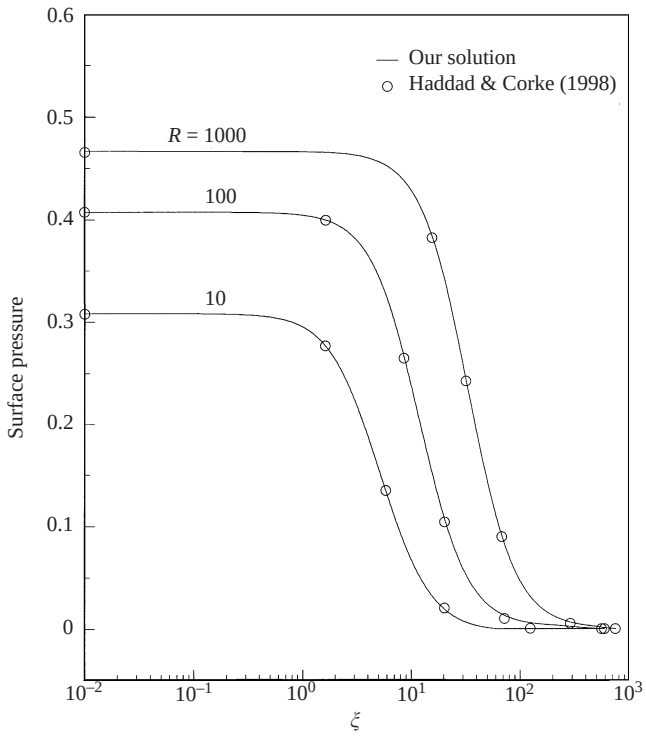

FIGURE 3. Pressure distribution on parabolic bodies.

downstream to asymptote to the Blasius solution. Based on this we are confident of their accuracy.

7.2. *Perturbation flow solutions*

7.2.1. *Sound at zero angle of incidence*

We first consider a zero sound incidence angle in order to make comparisons to the perturbation solution of Haddad & Corke (1998), and examine the Strouhal number scaling of the leading-edge receptivity.

In this study, the streamwise distance is denoted by a Reynolds number based on the surface arc length. The surface arc length along the parabolic body is given by

$$s(x) = \frac{R}{2}\left\{\left(1+\frac{2x}{R}\right)^{1/2}\left(2+\frac{2x}{R}\right)^{1/2} + \ln\left[\left(1+\frac{2x}{R}\right)^{1/2} + \left(2+\frac{2x}{R}\right)^{1/2}\right]\right\}. \quad (7.9)$$

Since we use a viscous length scale in non-dimensionalization, throughout this study s and Re_s are identical.

We non-dimensionalize the disturbance frequency such that σ is defined as

$$\sigma = \frac{2\pi f \nu}{U_\infty^2}. \quad (7.10)$$

We have examined frequencies ranging from $\sigma = 50.0 \times 10^{-6}$ to $\sigma = 120.0 \times 10^{-6}$. This range is shown with respect to the Blasius neutral curve in figure 4. The extent of the computational domain that figure shows that we encompass all of the linear amplified region for the full band of frequencies. For a physical reference

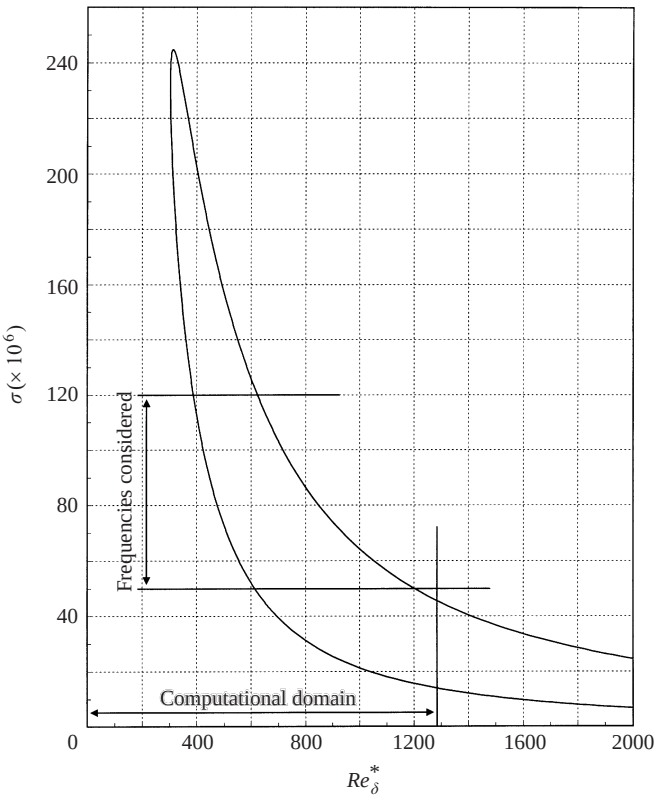

FIGURE 4. Neutral stability curve for Blasius boundary layer.

for comparison to experiments, in for example air, with $\nu = 1.5 \times 10^{-5}\,\mathrm{m^2\,s^{-1}}$ and a free-stream velocity $U_\infty = 6.7\,\mathrm{m\,s^{-1}}$, the dimensional frequencies will range between $f = 23.81$ and $f = 57.16\,\mathrm{Hz}$.

In order to verify our numerical solutions, a comparison with the results of Haddad & Corke (1998) was made. In their study, they only considered the conditions where the free-stream oscillations have a non-dimensional frequency of $\sigma = 230.0 \times 10^{-6}$, and a zero angle of incidence of sound, or $\alpha_2 = 0^\circ$. We compared our results at $R = 10$.

Figure 5 shows the magnitude of the perturbation vorticity on the wall with respect to the Reynolds number based on the surface arc length along the body. In this figure, the vorticity axis has been magnified in order to show the instability waves, in the linear amplified region. The spatial oscillations in the magnitude of the perturbation wall vorticity are clearly evident in the figure and there is excellent agreement with the previous results of Haddad & Corke (1998), shown as symbols.

There are a number of steps in the process of obtaining the leading-edge receptivity coefficient from the vorticity perturbation solution such as shown in figure 5. The first is to calculate the streamwise velocity perturbation, u, at different heights above the body surface. Examples of these at consecutive downstream locations are shown in figure 6, for $R = 100$, $\sigma = 120.0 \times 10^{-6}$, and $\alpha_2 = 0^\circ$.

The total streamwise velocity perturbation as seen in figure 6 is made up forced non-Orr–Sommerfeld modes, a Stokes wave, and T–S waves. Our interest is in the receptivity of the T–S wave, so that it was necessary to separate out the effect of

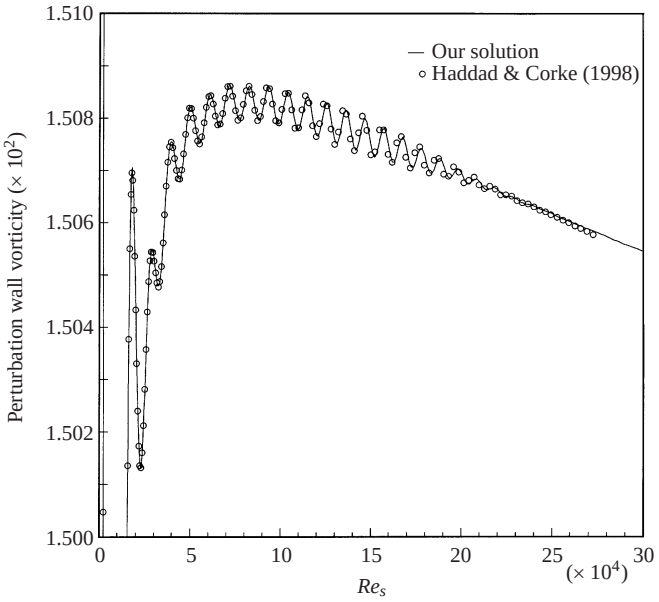

FIGURE 5. Enlarged view of perturbation wall vorticity along the surface; $R = 10$, $\sigma = 230 \times 10^{-6}$.

the other modes from the total perturbation solution. As a first step, we needed to subtract the Stokes wave from the total perturbation solution.

The Stokes flow is the natural response of the fluid to the free-stream oscillations and it is governed by the following equations:

$$\frac{\partial^2 \tilde{\psi}}{\partial \xi^2} + \frac{\partial^2 \tilde{\psi}}{\partial \eta^2} = -(\xi^2 + \eta^2)\tilde{\omega}, \tag{7.11}$$

$$-\mathrm{i}\sigma(\xi^2 + \eta^2)\tilde{\omega} + \frac{\partial^2 \tilde{\omega}}{\partial \xi^2} + \frac{\partial^2 \tilde{\omega}}{\partial \eta^2} = 0, \tag{7.12}$$

with the boundary conditions

$$\tilde{\psi} = 0, \quad \frac{\partial \tilde{\psi}}{\partial \eta} = 0, \quad \tilde{\omega} = \left(\frac{-1}{\xi^2 + \eta^2}\right)\frac{\partial^2 \tilde{\psi}}{\partial \eta^2} \quad \text{at} \quad \eta = R^{1/2}, \tag{7.13}$$

$$\frac{\partial \tilde{\psi}}{\partial \eta} = \xi \cos(\alpha_2) + \eta \sin(\alpha_2), \quad \tilde{\omega} = 0 \quad \text{at} \quad \eta = \eta_{max}, \tag{7.14}$$

where i is the imaginary number, σ is the frequency of the oscillations and α_2 is the angle of the free-stream acoustic waves. These equations are identical to the total perturbation flow equations without the convective terms. As such, the method of solution was identical to that of the perturbation flow equations. Figure 7 shows the u-profiles of the Stokes flow which corresponds to the conditions of figure 6.

To remove its effect, the Stokes flow solution was subtracted point by point from the total perturbation solution. An example of this is shown in figure 8, which again corresponds to the conditions in figure 6. As can be seen from figure 8, in the vicinity of the leading edge, the wall-normal u-distributions do not resemble a T–S eigenfunction. Near the leading edge, we suspect that the perturbation flow, after subtracting off the Stokes wave, is made up of a combination of forced (non-Orr–Sommerfeld) modes and T–S modes. Further downstream of the leading edge, for example at $Re_s = 438.7$,

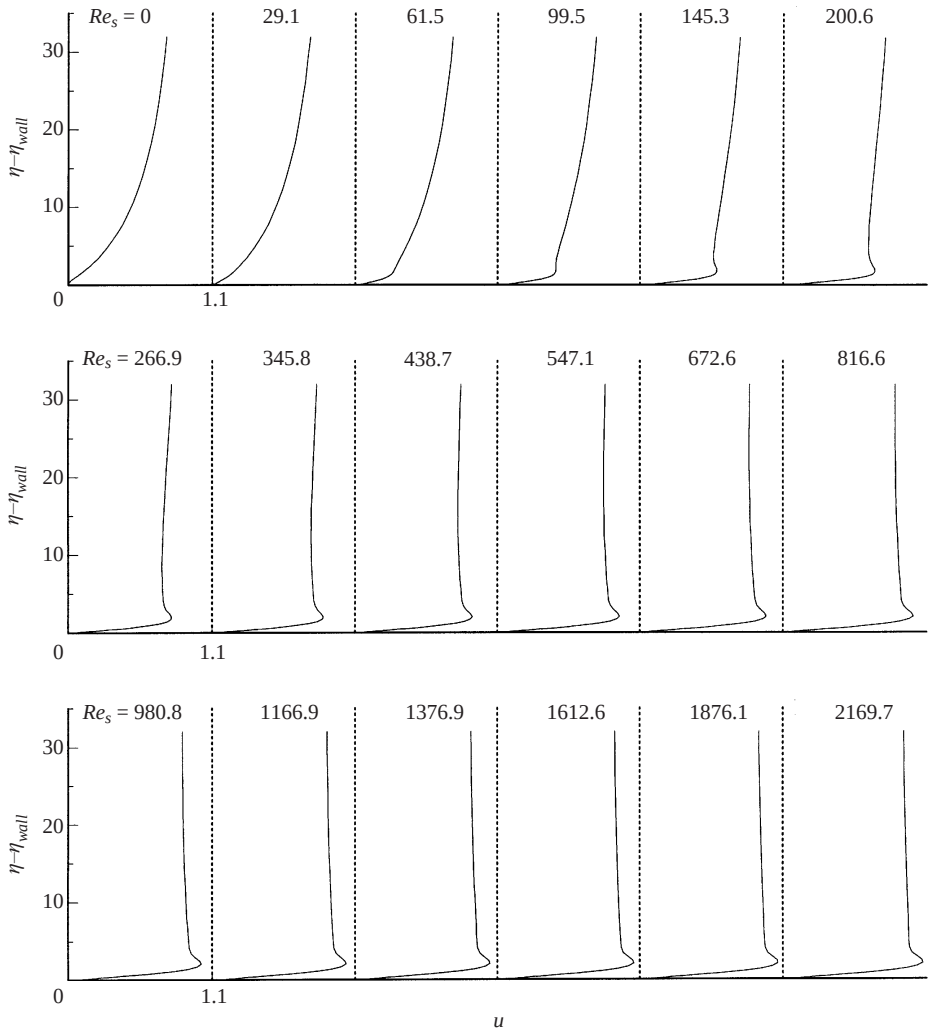

FIGURE 6. Total streamwise perturbation velocity profiles at consecutive downstream locations before Stokes wave is subtracted; $R = 100$, $\sigma = 120 \times 10^{-6}$.

the wall-normal streamwise velocity profiles eventually develop a T–S eigenfunction shape. Based on the lower peak in the wall-normal profile, we observe the amplitude to decrease with downstream distance. This is the expected behaviour since all of the locations shown in figure 8 are upstream of Branch I, which occurs at $Re_s \approx 149 \times 10^3$ for this frequency.

In this study, the receptivity coefficient is defined as the ratio of the maximum T–S amplitude at the leading edge, to the free-stream disturbance amplitude. This is referred to as $K_{LE} = |(u_{TS})_{LE}/u_\infty|$. Note that since we have already normalized the velocity perturbation with the free-stream velocity in the original formulation, the u-perturbation velocity profiles, such as shown in figure 8, correspond to the receptivity coefficient at their respective streamwise locations. The remaining step in obtaining the leading-edge receptivity coefficient is to extrapolate the value corresponding to T–S waves, upstream to the leading edge.

In figure 8 we observe that the maximum T–S amplitude (lower peak) occurs

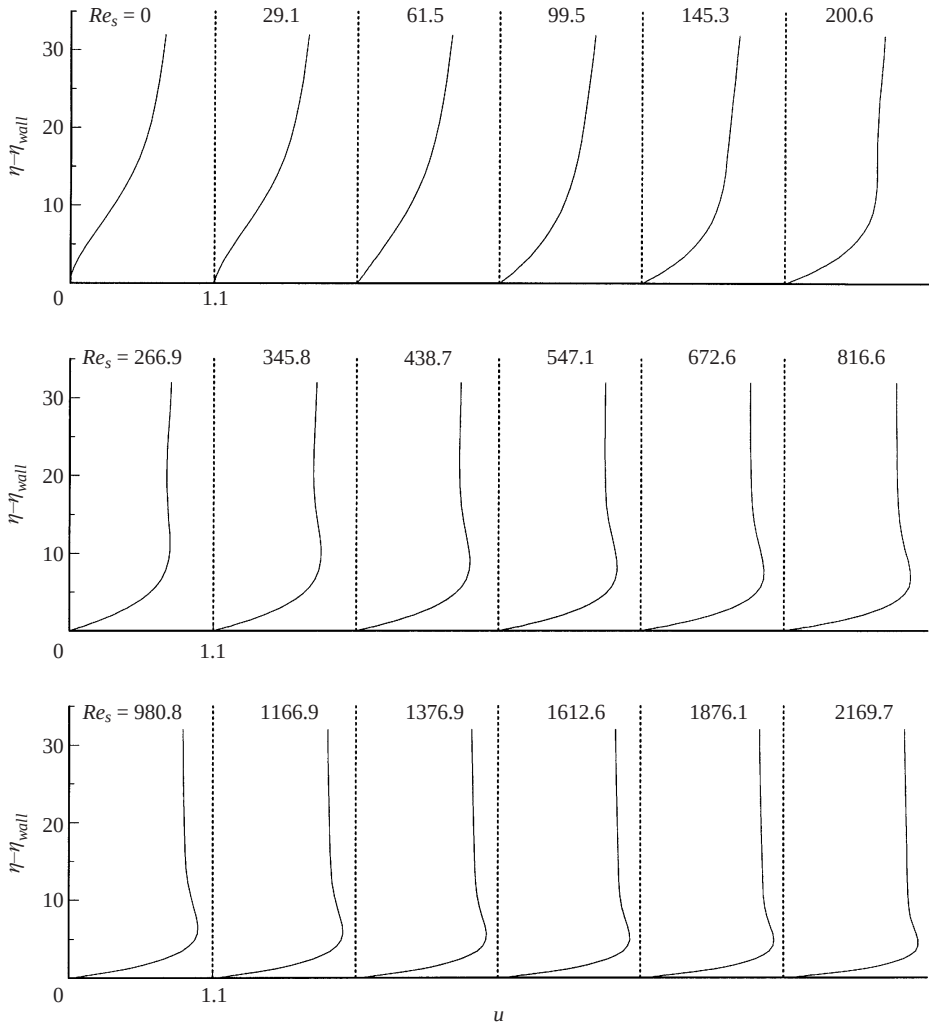

FIGURE 7. Streamwise velocity profiles of Stokes wave at consecutive downstream locations; $R = 100$, $\sigma = 120 \times 10^{-6}$.

at a constant η-position above the body surface. In order to get the receptivity coefficient at the leading edge, the u-amplitude at the η-position of the maximum, for distributions which had a T–S-like shape, were used to extrapolate from downstream positions, upstream to the leading edge. This is illustrated in figure 9, which shows the maximum T–S amplitude versus Re_s for two cases of leading-edge Reynolds number and free-stream frequency. Plot (a) has a linear scale for u. We expect that the T–S amplitude should decay exponentially, therefore to illustrate this better, the same data are plotted in figure 9(b) with u on a log axis. Based on plots like this, the exponential decay (linear in log scale) was best fit and used to extrapolate the T–S amplitude, and thereby receptivity coefficient, to the leading edge. Examples of the fit are shown as the solid curves through the data points in figure 9.

In their analytical study, Hammerton & Kerschen (1992) used a Strouhal number to represent the effect of leading-edge radius on receptivity. The Strouhal number is defined as $St = 2\pi f r_n/U_\infty$, where r_n is the leading-edge radius of curvature, and

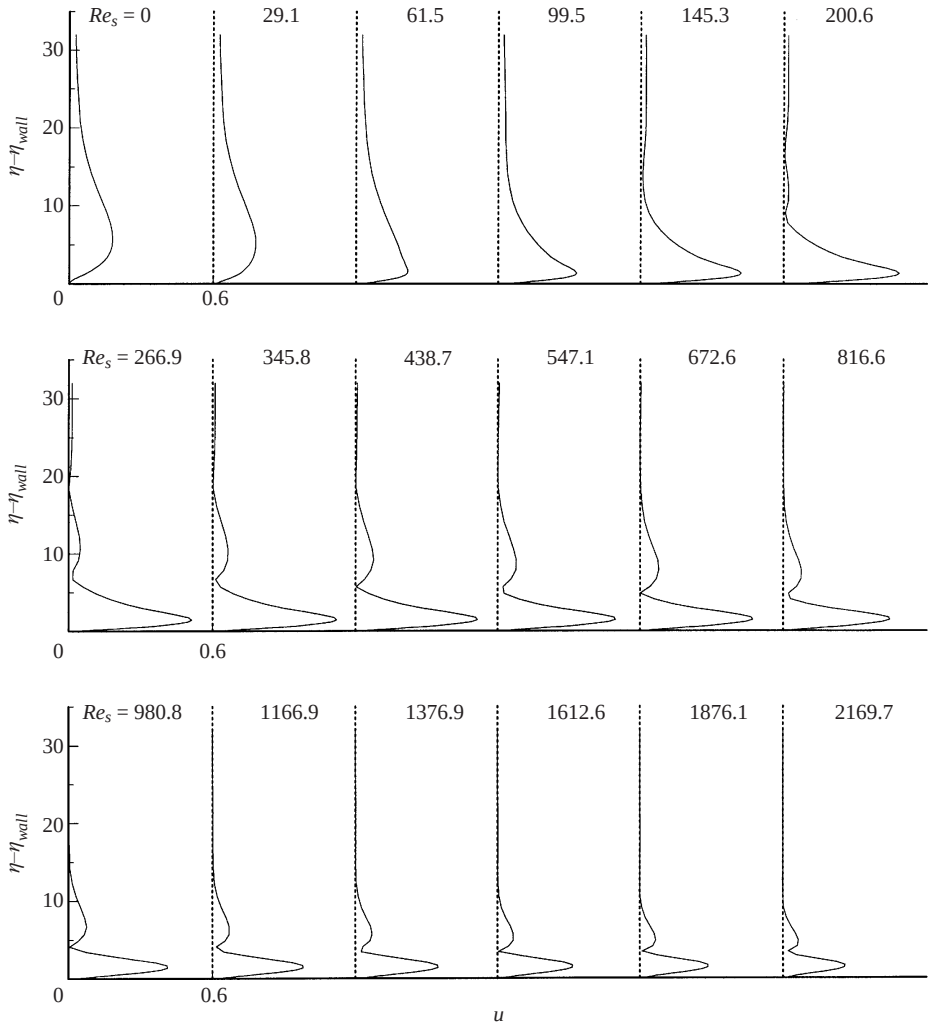

FIGURE 8. Streamwise perturbation velocity profiles at consecutive downstream locations after Stokes wave is subtracted; $R = 100$, $\sigma = 120 \times 10^{-6}$.

f is the dimensional frequency of the free-stream acoustic oscillations. Using our non-dimensional nose radius (R), and frequency (σ), the Strouhal number is simply $St = \sigma R$.

We decided to test the applicability of this Strouhal number, by varying the frequency and nose radius so that the Strouhal number remained the same. This is illustrated in figure 9, for two combinations in which $St = 0.012$. Clearly, although the T–S amplitude decay is different for the two frequency–radius combinations, the values of the leading-edge receptivity coefficient, which is found by extrapolating to $Re_s = 0$, are identical. Similar cases at different Strouhal numbers have verified it as an appropriate similarity variable for the leading-edge receptivity coefficient.

The effect of Strouhal number on the leading-edge receptivity coefficient is documented in figure 10: plot (*a*) used a linear scale for the receptivity coefficient, and plot (*b*) presents the receptivity coefficient on a log scale. These results are quantitatively similar to those of Haddad & Corke (1998), although the present results give slightly

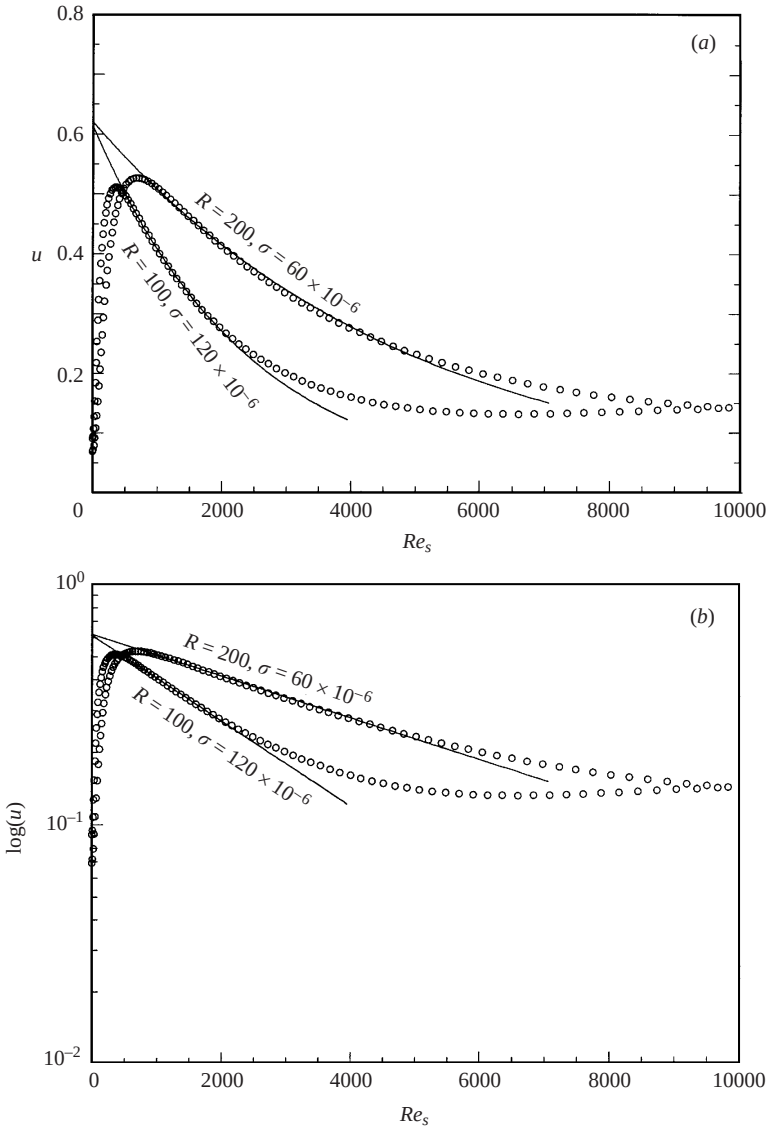

FIGURE 9. Comparison of the extrapolated leading-edge receptivity coefficient value obtained by using different nose Reynolds numbers and frequencies for a particular Strouhal number; $St = 0.012$.

larger K_{LE} at $St = 0$, and a slightly different decrease in K_{LE} with increasing St. The difference between the results of Haddad & Corke (1998) and the present results can be attributed to the uncertainty in the extrapolation of the decaying T–S amplitudes to the leading edge that was illustrated in figure 9. With the higher frequencies used by Haddad & Corke ($\sigma = 230.0 \times 10^{-6}$), the exponential decay is steeper, compared to the lower frequencies used here ($\sigma = 100.0 \times 10^{-6}$). As a result, the exponential fits and extrapolations used here are more accurate than in the previous study.

Hammerton & Kerschen (1992) stated that the decay of K_{LE} is exponential with respect to increasing St. We found this to be the case, as can be seen in figure 10(b), where the receptivity coefficient decreases almost exponentially (straight line) with Strouhal numbers greater than approximately 0.05.

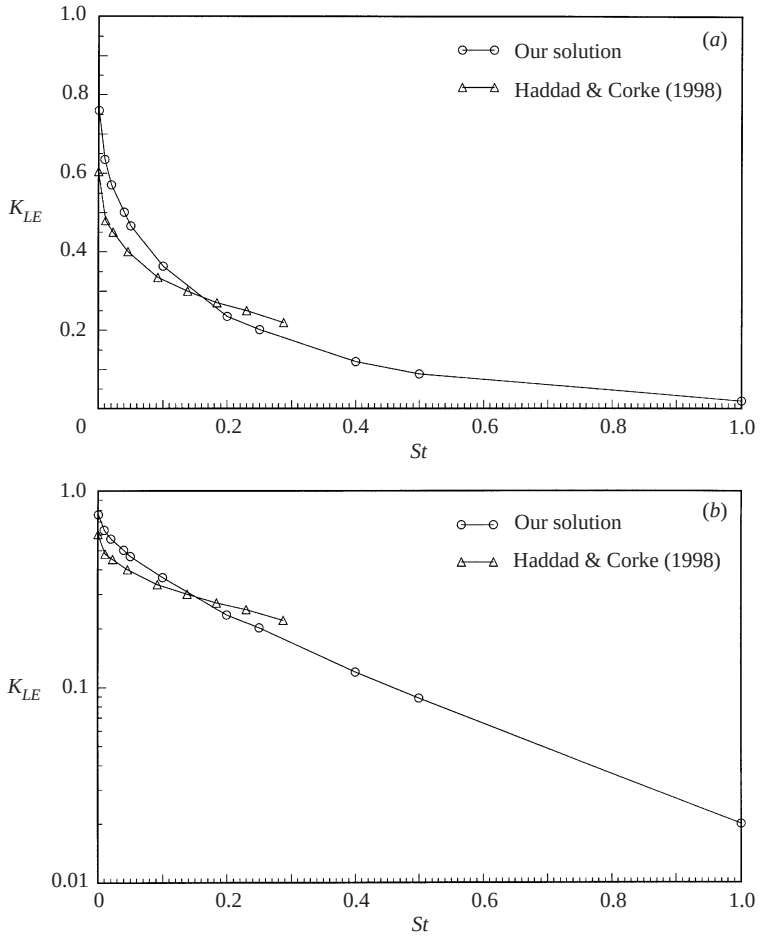

FIGURE 10. Variation of the leading-edge receptivity coefficient with Strouhal number.

7.2.2. *Sound at an angle of incidence*

To this point, all the results correspond to free-stream acoustic disturbances at a zero angle of incidence to the body ($\alpha_2 = 0$). The following results document the effect of a non-zero acoustic angle of incidence on the leading-edge receptivity coefficient.

Figure 11 demonstrates the effect of the angle of incidence of the acoustic waves on the amplitude of the instability waves near Branch II. This shows the u-perturbation velocity just above the wall for $R = 10$. The different cases correspond to incidence angle (α_2) of 0°, 10°, 20°, 90°, 110°, and 170° with respect to the body centreline. The oscillations in the u-velocity correspond to the T–S waves. If we draw an envelope connecting the peaks, its magnitude is indicative of the local receptivity coefficient. At the location of the maximum amplitude neutral growth point, the u value is by definition the Branch II receptivity coefficient, K_{II}. We observe that, as the angle of incidence of sound increases, up to 90°, K_{II} increases. Beyond an angle of 90°, K_{II} decreases. Qualitatively this agrees with our expectations based on the analysis of Hammerton & Kerschen (1996). However the receptivity coefficient at Branch II can be deceiving because it is also dependent on the pressure gradient from the leading edge to Branch II, which makes it body-specific. We therefore prefer to show the

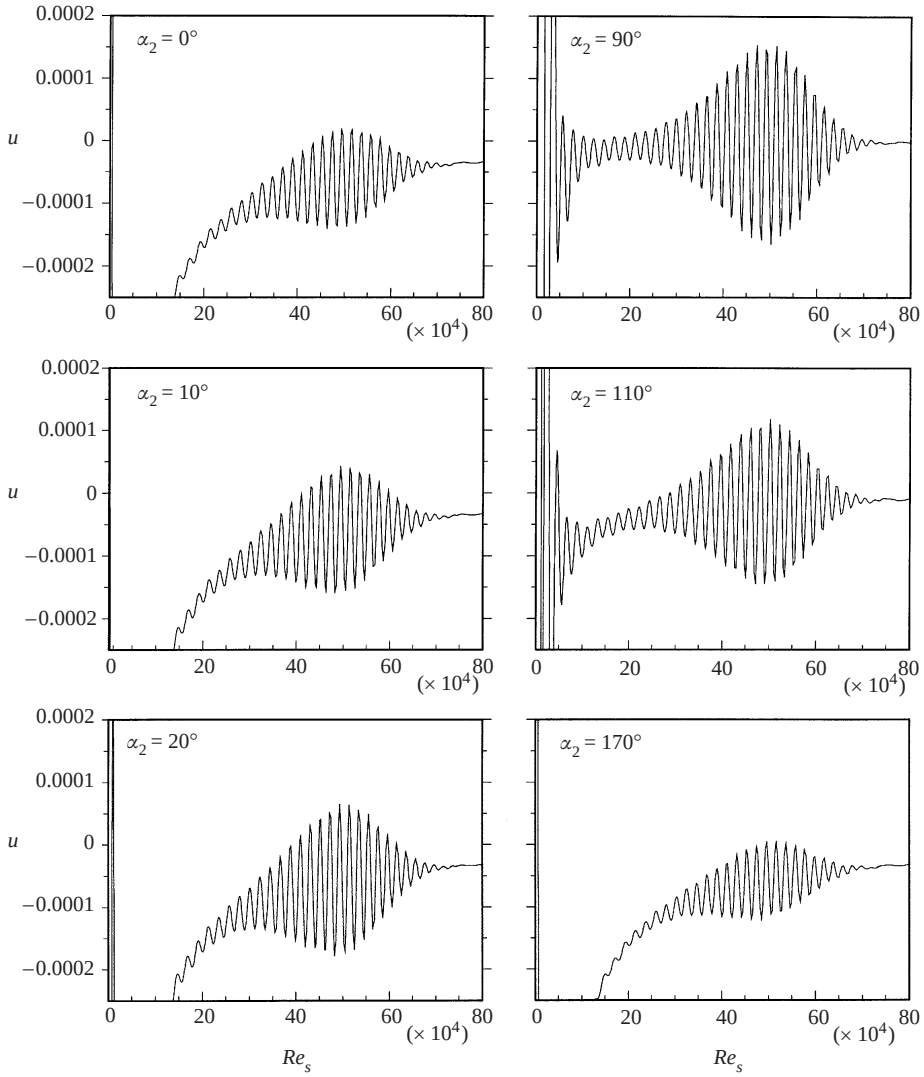

FIGURE 11. Streamwise variation of the u-velocity just above the wall near Branch I and II as a function of free-stream acoustic angle; $R = 10$, $\sigma = 100 \times 10^{-6}$.

effect of the angle of incidence of sound on the leading-edge receptivity coefficient, K_{LE}.

As before, the leading-edge receptivity coefficient was found by fitting an exponential function to the Re_s distribution of the maximum T–S amplitude. Figure 12 shows the streamwise variation of the u-perturbation velocity amplitude for the incidence angle (α_2) of 0°, 60°, 90°, 120°, 150°, and 170° for $R = 10$. The solid lines are the exponential fit used in extrapolating to the leading edge. This shows that K_{LE} increase as α_2 increases up to $\alpha_2 = 90°$, and then decreases for larger angles, in a manner which was previously observed with K_{II}.

One of the interesting aspects of the streamwise variation in the u-perturbation is the appearance of a local minimum at the larger angles of incidence, for example at $\alpha_2 = 120°$ and 150° in figure 12. Since the governing equations for the perturbation

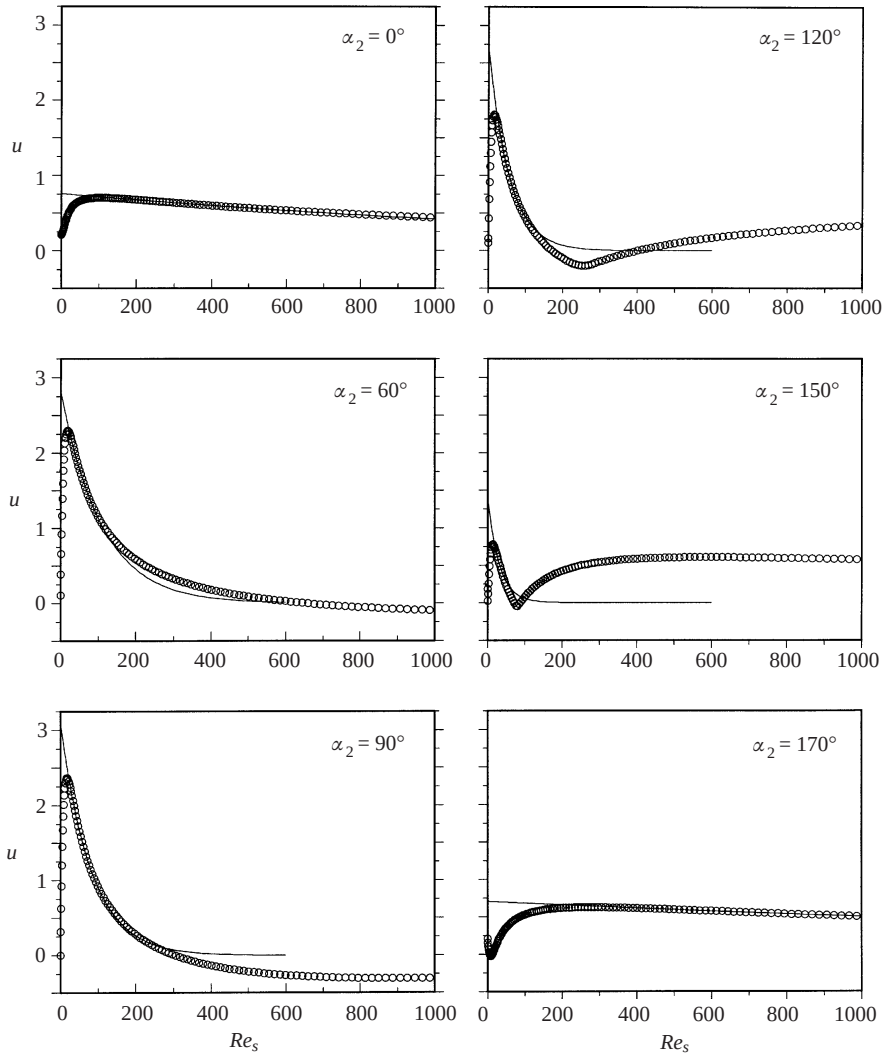

FIGURE 12. Streamwise variation of the maximum u-velocity near the leading edge as a function of free-stream acoustic angle; $R = 10$, $\sigma = 100 \times 10^{-6}$.

flow are linear, we considered that the local minimum might be the result of a linear phase change. To investigate this, we plotted the corresponding phase difference between the free-stream oscillations and the Stokes-removed u-perturbations at the wall-normal amplitude maximum. This is shown for $\alpha_2 = 120°$ and $150°$ in figure 13(a) and 13(b).

The phase distribution documents that the amplitude minimum in these cases does correspond to a 180° phase shift. This suggests that the amplitude minimum results from a linear phase cancellation mechanism. However we do not know precisely the source of the phase change. Wall-normal profiles of the u-perturbation for $\alpha_2 = 120°$ in figure 14 show that a characteristic change occurs near the location of the streamwise phase change ($Re_s \approx 200$). Upstream of that location ($Re_s < 60$), the wall-normal profile has a two-peaked shape which is characteristic of a T–S eigenfunction. Near $Re_s \approx 200$, the wall-normal profile has a three-peaked shape,

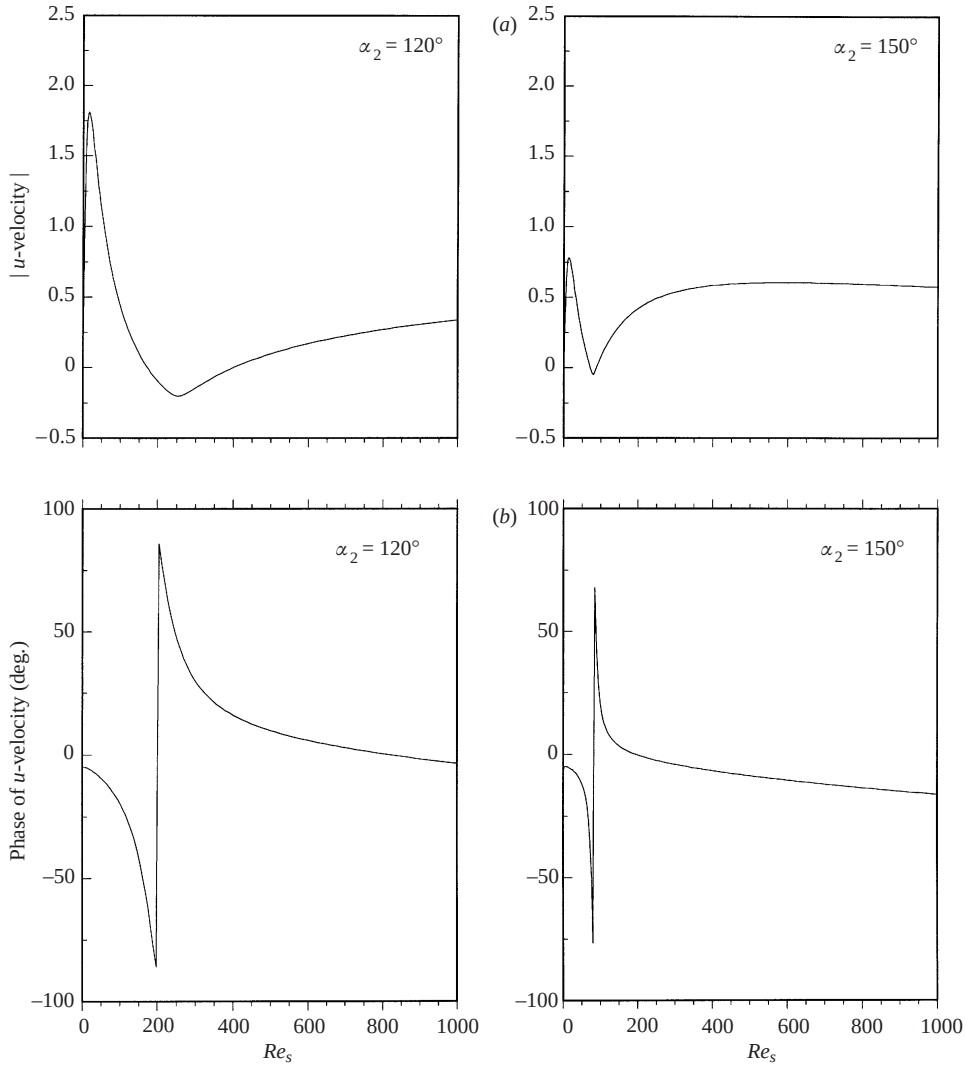

FIGURE 13. The minimum in (*a*) streamwise *u*-velocity magnitude distribution and (*b*) the streamwise *u*-velocity phase distribution; $R = 10$, $\sigma = 100 \times 10^{-6}$.

with a minimum occurring at the previous (upstream) location of the wall-normal distribution maximum. Downstream of this location, the amplitude maximum returns to its original upstream location above the wall.

An additional observation is that the streamwise location of the phase change moves upstream with increasing angle of incidence of sound. At $\alpha_2 = 170°$ in figure 12, it appears to be virtually at the leading edge.

These results prompted us to only use the streamwise region which was upstream of the phase change to extrapolate to the leading edge for determining K_{LE} in these cases. For the large values of α_2, the shorter region for the exponential fit increased somewhat the uncertainty of the leading-edge value.

A compilation of the leading-edge receptivity coefficients for the full range of sound incidence angles, for three different nose-radius Strouhal numbers is shown in figure 15. This shows clearly that K_{LE} increases as the sound angle of incidence

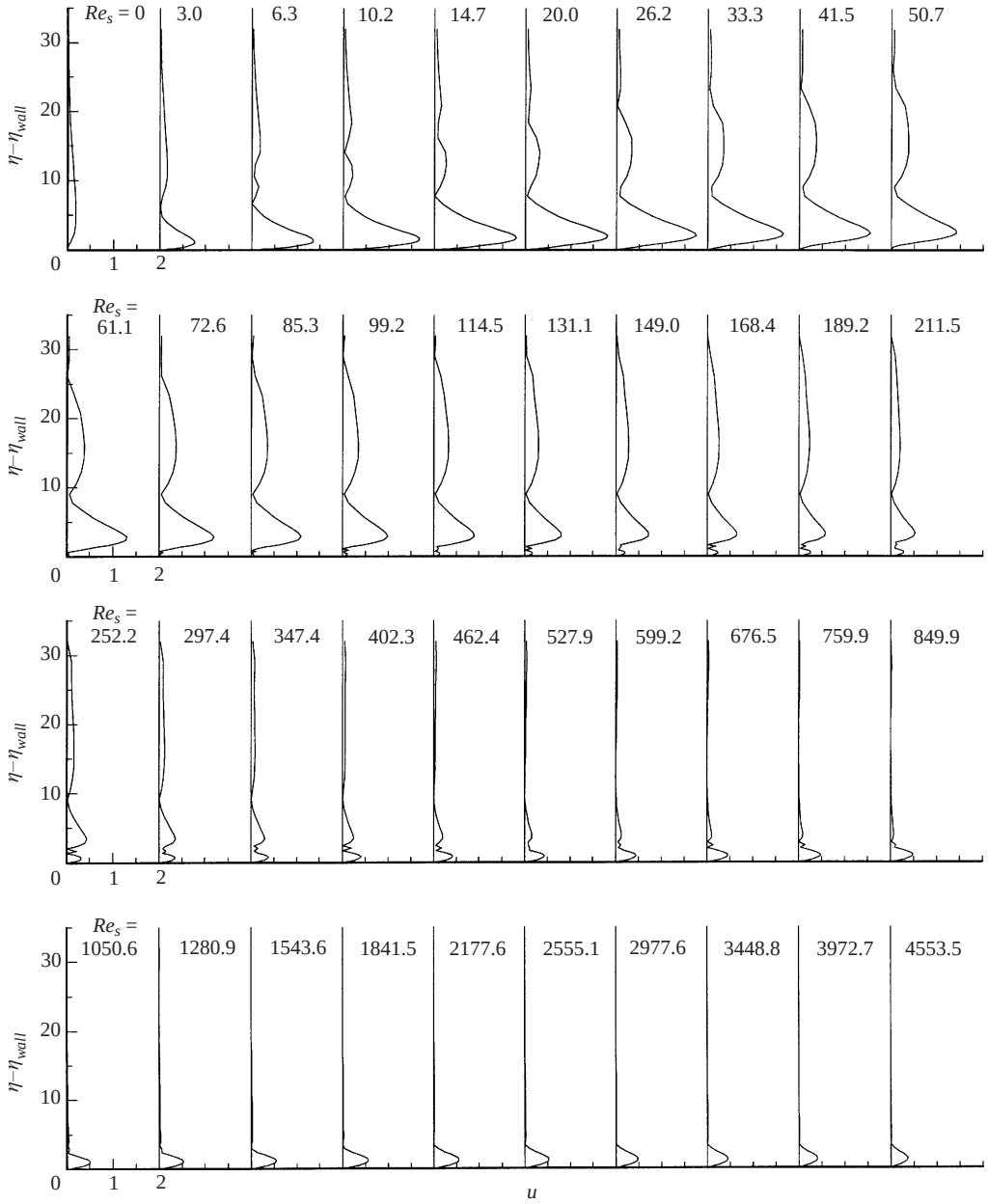

FIGURE 14. Profiles of u-perturbation velocity at consecutive downstream locations at free-stream acoustic angle of $\alpha_2 = 120°$; $R = 10$, $\sigma = 100 \times 10^{-6}$.

increases in the range $0° \leqslant \alpha_2 \leqslant 90°$. The maximum receptivity coefficient occurs at $\alpha_2 = 90°$. In addition, the variation of the leading-edge receptivity coefficient with sound angle is not symmetric about the 90° angle. This is most evident near the minima in the K_{LE}. Rather than being at $\alpha_2 = 0°$ and 180°, the minimum occurs at $\alpha_2 = -10°$ and 170°. This result agrees with the analysis of Hammerton & Kerschen (1996), which showed the same kind of asymmetry for small reduced frequencies. In their case, it was seen as a balance between symmetric and antisymmetric components,

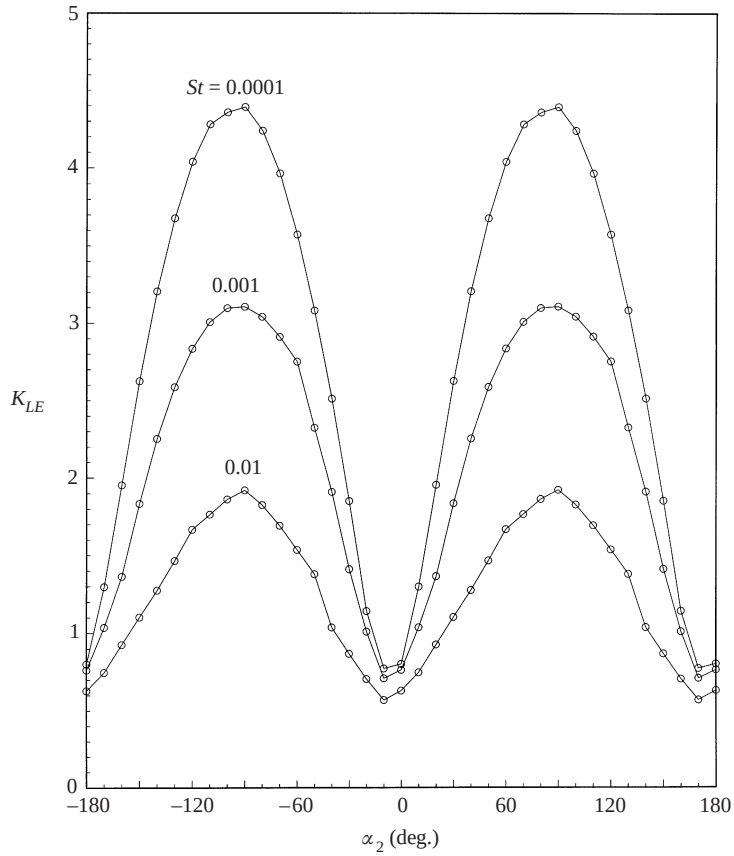

FIGURE 15. Variation of the leading-edge receptivity coefficient with respect to the angle of the acoustic wave as a function of Strouhal number.

$\cos(\alpha_2)$ and $a^{1/2}\sin(\alpha_2)$ respectively, where a is an aerodynamic reduced frequency. Except near $\alpha_2 = 0^\circ$ and 180°, the antisymmetric component is dominant, as we observed here.

The variation of K_{LE} with sound angle is not dependent on the nose-radius Strouhal number. The only effect is that the smaller radius (smaller Strouhal number) has a larger receptivity coefficient, regardless of the sound angle. This is of course consistent with the results in figure 10.

An interesting aspect of the asymmetry of the K_{LE} with changing acoustic angle is illustrated in figure 16. This shows the streamwise amplitude variation of the u-perturbation maximum on either side of the leading edge for $\alpha_2 = 10^\circ$, 0°, and -10°. These are similar to those in figure 9, which only showed the variation on the upper surface (positive-ξ side). Of course, these distributions are used to extrapolate to the leading edge to obtain K_{LE}. When $\alpha_2 = 0^\circ$, the value obtained by extrapolating from the lower surface or upper surface is the same. However, at a small sound angle of 10°, the value extrapolated from the lower surface is different from that extrapolated from the upper surface. In this case with $\alpha_2 = 10^\circ$, the value extrapolated from the lower surface equals the one extrapolated from the upper surface at $\alpha_2 = -10^\circ$. This asymmetry exists at all angles but 0° and 90°. It is most pronounced near $\alpha_2 = 0^\circ$ and 180°.

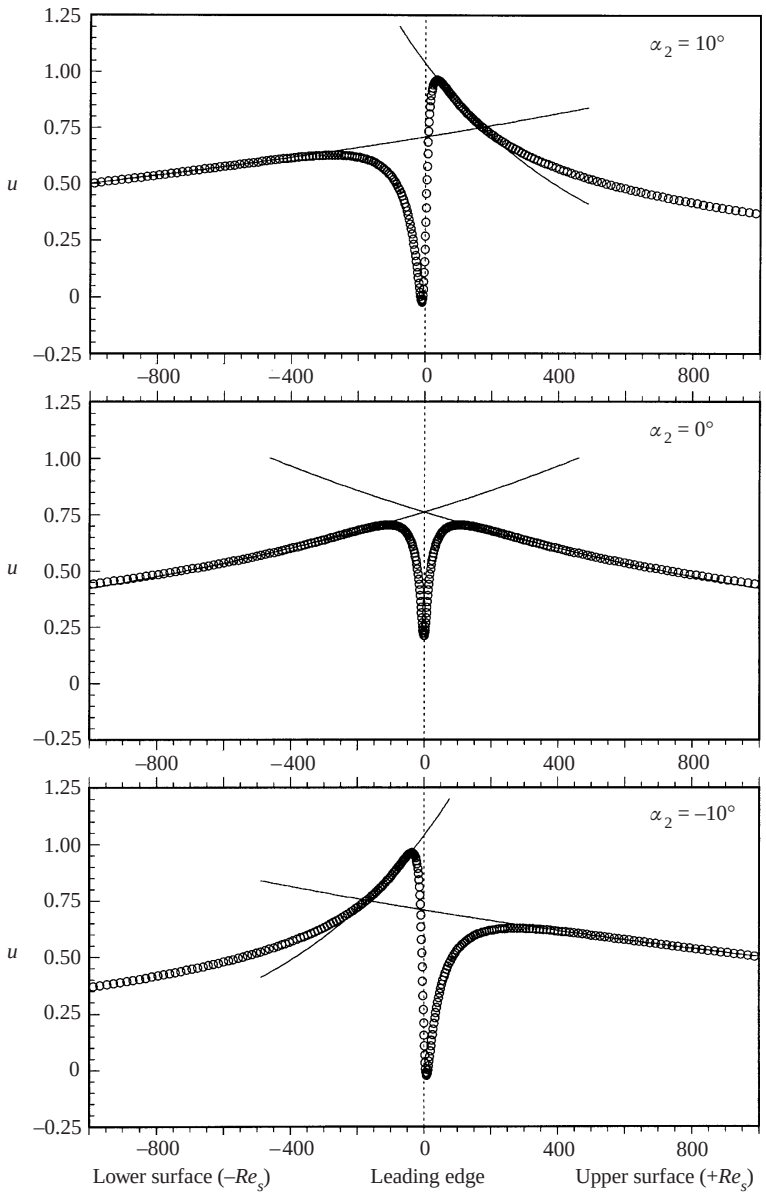

FIGURE 16. Amplitude distribution of the instability waves on both the upper and lower surfaces of the parabola.

8. Conclusions

The spatial formulation used in this problem was successful in modelling the evolution of the T–S instability induced by acoustic free stream disturbances at various angles of incidence. For these, we found that the Strouhal number defined as $St = 2\pi f r_n / U_\infty$ was a correct similarity variable for the leading-edge receptivity coefficient dependence on the nose radius of curvature. This agreed with the analysis of Hammerton & Kerschen (1992).

The leading-edge receptivity coefficient increased as the Strouhal number decreased. This again agreed with the analysis of Hammerton & Kerschen (1992) and the

previous computations of Haddad & Corke (1998). The variation of K_{LE} with Strouhal number was found to be exponential for $St > 0.05$.

The results showed that the leading-edge receptivity coefficient increased with increasing angle of incidence of sound, up to 90°. For angles greater than 90°, it decreased. The minimum receptivity did not occur at angles of 0° and 180°, but slightly shifted to values of −10° and 170° respectively. This result in an asymmetry between the leading-edge receptivity coefficient based on an extrapolation to the leading edge of the T–S amplitudes on the upper or lower surfaces of the body. This asymmetry was predicted in the analysis of Hammerton & Kerschen (1996) for small reduced frequencies.

With higher angles of sound, we observed a sharp minimum in the streamwise development of the Stokes-removed *u*-perturbation slightly downstream of the leading edge. This minimum was found to coincide with a 180° phase shift in the *u*-perturbation phase. This suggests that the amplitude minimum is caused by a linear interaction between modes, most likely T–S and non-Orr–Sommerfeld (forced) modes. This is supported by wall-normal distributions, which in the vicinity of the streamwise amplitude minimum develop a peak nearer to the wall. The exact implication of this is unknown, although this minimum was observed to move upstream as the sound angle increased, and it was virtually at the leading edge when the angle was 170°. The sound angle of 170° (and its complement, −10°) was approximately the value that produced the minimum leading-edge receptivity.

Overall we found very good quantitative agreement with the previous computations of Haddad & Corke (1998), which were for a more limited frequency range and with a zero sound incidence angle. The differences in the geometry, semi-infinite in our case versus finite, only allowed qualitative comparisons between our receptivity coefficients and those from the analysis of Hammerton & Kerschen (1996). However overall we found excellent qualitative agreement which suggests that we agreed in the essential physics of the acoustic receptivity process.

E. Erturk is grateful for the financial support of the Gebze Institute of Technology through the funds of the Turkish Council of Higher Education while conducting this research.

REFERENCES

Anderson, D. A., Tannehill, J. C. & Pletcher, R. H. 1984 *Computational Fluid Mechanics and Heat Transfer*. McGraw-Hill.

Davis, R. T. 1972 Numerical solution of the Navier–Stokes equations for symmetric laminar incompressible flow past a parabola. *J. Fluid Mech.* **51**, 417–433.

Erturk, E. 1999 Leading edge boundary layer receptivity to oblique free stream acoustic waves on parabolic bodies. PhD Thesis, Illinois Institute of Technology, Chicago.

Erturk, E. & Corke, T. C. 2001 An efficient numerical method for steady incompressible Navier–Stokes equations and driven cavity flow at very high Reynolds numbers. *J. Comput. Phys.* (submitted).

Goldstein, M. E. 1983 The evolution of Tollmien–Schlichting waves near a leading edge. *J. Fluid Mech.* **127**, 59–81.

Haddad, O. M. & Corke, T. C. 1998 Boundary layer receptivity to free-stream sound on parabolic bodies. *J. Fluid Mech.* **368**, 1–26.

Hammerton, P. W. & Kerschen, E. J. 1992 Effect of nose bluntness on leading-edge receptivity. In *Instability, Transition and Turbulence* (ed. M. Y. Hussaini, A. Kumar & C. L. Streett), p. 421. Springer.

Hammerton, P. W. & Kerschen, E. J. 1996 Boundary-layer receptivity for a parabolic leading edge. *J. Fluid Mech.* **310**, 243–267.

Lin, N., Reed, H. L. & Saric, W. S. 1990 Leading edge receptivity to sound: Navier–Stokes computations. *Appl. Mech. Rev.* **43**, S175.

Morkovin, M. V. 1969 On the many faces of transition. In *Viscous Drag Reduction.* Plenum

Murdock, J. W. 1981 Tollmien–Schlichting waves generated by unsteady flow over parabolic cylinders. *AIAA Paper* 81–0199.

Saric, W. S., Wei, W. & Rasmussen, B. K. 1994 Effect of leading edge on sound receptivity. In *Laminar-Turbulent Transition IV, Proc. IUTAM Symp. Sendai, Japan* (ed. R. Kobayashi).